Physics of Fluids

Effects of nutrient depletion on tissue growth in a tissue engineering scaffold pore

Cite as: Phys. Fluids **33**, 121903 (2021); https://doi.org/10.1063/5.0071171
Submitted: 12 September 2021 • Accepted: 31 October 2021 • Published Online: 02 December 2021

Zeshun Zong (宗泽舜), **Xinyu Li** (李新宇) and **Pejman Sanaei**

Physics of Fluids ARTICLE scitation.org/journal/phf

Effects of nutrient depletion on tissue growth in a tissue engineering scaffold pore

Cite as: Phys. Fluids 33, 121903 (2021); doi: 10.1063/5.0071171
Submitted: 12 September 2021 · Accepted: 31 October 2021 ·
Published Online: 2 December 2021

Zeshun Zong (宗泽舜),[1] Xinyu Li (李新宇),[2] and Pejman Sanaei[3,a)]

AFFILIATIONS

[1]Mathematics Department, University of California, Los Angeles, Los Angeles, California 90095, USA
[2]Industrial Engineering and Operations Research, University of California, Berkeley, Berkeley, California 94720, USA
[3]Department of Mathematics, New York Institute of Technology, New York, New York 10023, USA

[a)]Author to whom correspondence should be addressed: psanaei@nyit.edu. URL: https://sites.google.com/nyit.edu/pejman-sanaei-webpage

ABSTRACT

In a tissue engineering scaffold pore lined with cells, nutrient-rich culture medium flows through the scaffold and the cells proliferate. In this process, both environmental factors—such as flow rate and shear stress—as well as cell properties have significant effects on tissue growth. Recent studies have focused on the effects of scaffold pore geometry on tissue growth, while in this work, we focus on the nutrient depletion and consumption rate by the cells, which cause a change in the nutrient concentration of the feed and influence the growth of cells lined downstream. In this paper, our objectives are threefold: (i) design a mathematical model for the cell proliferation describing fluid dynamics, nutrient concentration, and tissue growth; (ii) solve the models and then simulate the tissue proliferation process; (iii) design a "reverse algorithm" to find the initial configuration of the scaffold with the knowledge of the desired property of the final tissue geometry. Our model reduces the numerical burdens and captures the experimental observations from the literature. In addition, it provides an efficient algorithm to simulate the cell proliferation and determine the design of a tissue engineering scaffold given a desired tissue profile outcome.

I. INTRODUCTION

Tissue engineering, which is the culturing of artificial tissue outside human body in order to replace damaged tissues and organs, has been widely used for clinical therapies.[1,2] In this process, both environmental factors—such as flow rate and shear stress—and the cell property have significant effects on tissue growth. Previous works have discussed the effects of external factors on tissue growth, including fluid mechanical forces with a focus on shear stress and pressure,[3–6] as well as the scaffold geometric design.[7–11] In addition, many mathematical models of tissue growth have been built to provide simulations on the final shape and the pore-filling process.[12,13] While most of the focus has been devoted to the influences of the external environment such as the fluid dynamics and the scaffold geometric design, less attention has been given to the effects of cell behavior. Note that, as cells consume nutrients, the nutrient concentration in the flow changes. In particular, as cells at the top of the scaffold pore consume nutrients, the concentration of nutrient solution will be lower at the bottom of the scaffold pore, which in turn results in a slower growth rate for cells at the downstream side. Therefore, both the final scaffold pore geometry and the total amount of tissue growth are influenced. Previous works did not reveal the influence of this factor.[7,14,15]

Numerous mathematical models have been developed by researchers to study the mechanism of cell proliferation in a tissue engineering scaffold. For example, Kumar *et al.*[16–18] introduced models for a deformable cylindrical scaffold and neglected the effects of nutrient depletion along the depth of the scaffold. In addition, the researchers[17] provided a semi-analytical solution for a short period of time. Sanaei *et al.*[14] proposed a mathematical model for tissue engineering in the context of a single pore of a scaffold. The authors considered the combined roles of fluid shear stress and geometry curvature of a scaffold pore on the tissue growth and investigated how these factors influence the total tissue growth in a scaffold pore. A critical assumption of all of the above-mentioned works[7,14–17] is that the nutrient concentration is assumed to be constant throughout the scaffold pore. In reality, however, the assumption does not hold. As cells begin to consume nutrients, the concentration decreases and influences the cells' growth rate at the downstream side of the scaffold. In this work, we develop a model and introduce a parameter named "hunger rate" to determine the homogeneous nutrient depletion rate of cells in

a tissue engineering scaffold. We focus on the homogeneous property of cells in the scaffold and assume that each individual cell in the scaffold would consume nutrients at the same hunger rate. In this way, we are able to compare the final geometries and the growth processes of different kinds of cells with different hunger rates.

Another innovative part of our work is the implementation of a "reverse algorithm," which is used to design the initial configuration of the tissue engineering scaffold. Though there are several mathematical models to predict the tissue growth process and provide spatiotemporal information on the scaffold pore final shape,[14,19,20] very few have been devoted to designing tissue engineering scaffolds (see Refs. 21–24 and references therein). They mostly used comprehensive parametric variation study to design and optimize the tissue engineering scaffold. Specifically, what is missing from the literature is a model adopting a predictive algorithm using first principles for optimizing and designing the initial configuration of the tissue engineering scaffold based on the final desired tissue geometry. For practical use, however, a correct initial configuration of the scaffold could be very critical.[8,25] By incorporating the nutrient concentration and fluid dynamics, the algorithm is able to return a precise three-dimensional scaffold design efficiently.

This paper is structured as follows: in Sec. II, we introduce the mathematical model incorporating three parts—the governing equations for fluid dynamics through a single pore of a tissue engineering scaffold in Sec. II A; the rate of change of the nutrient concentration and its boundary conditions in Sec. II B; and the partial derivative equations governing tissue growth in Sec. II C. We perform nondimensionalization of the models in Sec. III and then apply asymptotic and quasi-static analysis to solve the partial differential equations in Sec. IV, where we utilize the fact that the aspect ratio of the pore is small and the timescale of cell proliferation is much longer compared to that of nutrient flow transport. The results are shown in Sec. V and we present the reverse algorithm and initial configuration. Finally, we conclude in Sec. VI with a discussion of our model and results with potential future improvements.

II. MODEL DESCRIPTION

We consider a simple continuum model, in which the scaffold consists of a series of identical nearly cylindrical pores spanning the entire scaffold, with depth-dependent radius shown in Fig. 1. Therefore, we focus on a single scaffold pore, with cells initially lined on the pore wall and nutrient solution flows through the pore. As time passes, the cells proliferate and the fluid–cell–layer shrinks as the tissue layer thickens. As a result, the shape and structure of the pore changes, so do the nutrient concentration, shear stress, etc. We consider a quasi-static assumption, which stems from the fact that the tissue growth happens on a much longer timescale compared to that of the transport of the fluid flow through the scaffold pore.[8,14]

Since the shape of the scaffold is fixed throughout the paper, we primarily consider the change of the shape of fluid–cell–layer, which represents the growth of tissue. Let $\hat{L}$ and $\hat{R}$ denote the length and the typical pore radius, respectively, and, hence, also the length and radius of the fluid–cell–layer at the initial state, since we assume initially the thickness of cell sources is negligible. The aspect ratio ϵ is defined to be $\epsilon = \hat{R}/\hat{L} \ll 1$. The geometry of the underlying substrate is assumed to be nearly circularly cylindrical with small azimuthal and axial variation, which later would be viewed as a control for optimization of the tissue growth.

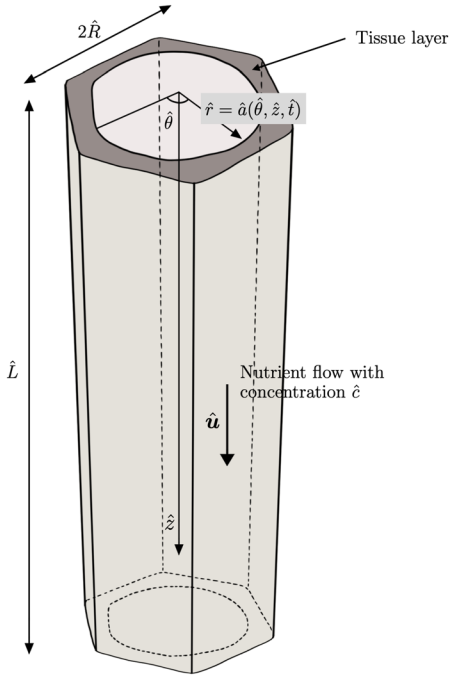

FIG. 1. Schematic diagram of a possible geometry of a tissue-lined pore within a tissue engineering construct.

The concentration of nutrient solution is allowed to change throughout the length of pore, due to nutrient consumption by the cells at the pore wall. We assume, as in many real world applications, that the inlet flux and concentration of fluid supplied to the cells are held constant.[26,27] Intuitively, if the rate of nutrient consumption is low, which we will characterize by the "hunger rate" $\hat{\eta}$, then our model should resemble the case considered in Ref. 14 so that the nutrient is in excess. As in Ref. 14, we prescribe the influx $\hat{Q}_i$ and zero downstream pressure. The nutrient fluid is modeled as an incompressible Newtonian viscous fluid with viscosity $\hat{\mu}$ and density $\hat{\rho}$.

The system is constructed in cylindrical coordinates $(\hat{r}, \theta, \hat{z})$, where the vertical axis $\hat{z}$ is aligned with the pore axis and $\boldsymbol{e}_{\hat{r}}, \boldsymbol{e}_\theta, \boldsymbol{e}_{\hat{z}}$ are the unit vectors in $\hat{r}, \theta, \hat{z}$ directions, respectively. Let $\hat{r} = \hat{a}(\theta, \hat{z}, \hat{t})$ describe the fluid–cell–layer interface, where the initial configuration is given by $\hat{r} = \hat{a}(\theta, \hat{z}, 0)$ as shown in Fig. 1.

A. Fluid dynamics

We denote the velocity of the fluid and the pressure across the pore as $\hat{\boldsymbol{u}} = \hat{u}\boldsymbol{e}_{\hat{r}} + \hat{v}\boldsymbol{e}_\theta + \hat{w}\boldsymbol{e}_{\hat{z}}$ and $\hat{p}$, respectively. Experiments and literature reports have shown that the inertial force is negligible;[28,29] therefore, we assume that the flow is governed by the Stokes equations subject to no-slip and no-penetration boundary conditions. The mechanics of the flow are therefore characterized by

$$\hat{\nabla}\hat{p} = \hat{\mu}\hat{\nabla}^2\hat{\boldsymbol{u}}, \quad \hat{\nabla}\cdot\hat{\boldsymbol{u}} = 0, \tag{1}$$

with boundary conditions

$$\hat{\boldsymbol{u}}|_{\hat{r}=\hat{a}} = 0, \quad \hat{u}|_{\hat{r}=0} = \hat{v}|_{\hat{r}=0} = \left.\frac{\partial \hat{w}}{\partial \hat{r}}\right|_{\hat{r}=0} = 0, \tag{2}$$

where $\hat{\mathbf{V}}$ is the dimensional gradient operator. Throughout the procedure, we assume that the total flux passing through the pore is held constant to keep a continued nutrient supply, i.e.,

$$\int_0^{2\pi}\int_0^{\hat{a}} |\hat{\boldsymbol{u}}|\,\hat{r}\,d\hat{r}\,d\hat{\theta} = \hat{Q}_i = \text{constant}. \tag{3}$$

As the pore radius shrinks, the pressure difference needs to increase in order to sustain the flux. We therefore prescribe the pressure at the top and the channel downstream as follows:

$$\hat{p}|_{\hat{z}=0} = \hat{\zeta}(\hat{t}), \quad \hat{p}|_{\hat{z}=1} = 0, \tag{4}$$

where $\hat{\zeta}(\hat{t})$ is a function, which is monotonically increasing with time $\hat{t}$. In addition, the total shear stress $\hat{\sigma}_s$ at the channel wall, exerted by the nutrient flow, is obtained from the following expressions:

$$\hat{\sigma}_s = \sqrt{|\hat{\boldsymbol{\sigma}}\boldsymbol{n}|^2 - ((\hat{\boldsymbol{\sigma}}\boldsymbol{n})\cdot\boldsymbol{n})^2}, \quad \hat{\boldsymbol{\sigma}} = \mu\left(\hat{\mathbf{V}}\hat{\boldsymbol{u}} + \hat{\mathbf{V}}\hat{\boldsymbol{u}}^T\right)|_{\hat{r}=\hat{a}}, \tag{5}$$

where T shows the transpose of the matrix and $\boldsymbol{n}$ is the unit vector normal to the fluid–cell–layer interface, pointing inward, given by

$$\boldsymbol{n} = \frac{\hat{\mathbf{V}}(\hat{r}-\hat{a})}{|\hat{\mathbf{V}}(\hat{r}-\hat{a})|}. \tag{6}$$

B. Nutrient concentration

We assume that the nutrient is diluted in fluid flow with concentration $\hat{c}$. The rate of change of the nutrient concentration $\hat{c}$ satisfies

$$\frac{\partial \hat{c}}{\partial \hat{t}} = \hat{\nabla}\cdot\hat{\mathbf{Q}}_n, \tag{7}$$

where

$$\hat{Q}_n = -\hat{\Xi}\hat{\nabla}\hat{c} + \hat{u}\hat{c} \tag{8}$$

is the nutrient flux, with $\hat{\Xi}$ being the diffusion coefficient of the nutrient.[30–32] The initial condition for the nutrient concentration within the channel follows

$$\hat{c}|_{\hat{t}=0} = 0, \quad 0 \le \hat{r} \le \hat{a}|_{\hat{t}=0}, \quad 0 \le \hat{\theta} \le 2\pi, \quad 0 < \hat{z} \le L. \tag{9}$$

Note that, by employing the quasi-static assumption for (7), the initial condition for the nutrient concentration given in (9) will not be needed for further analysis of our model. This will be explained in detail in Sec. III B. Nutrient concentration should also satisfy the following boundary conditions:[30–32]

$$\begin{aligned} &\hat{c}|_{\hat{z}=0} = \hat{c}_i, \quad \left.\frac{\partial \hat{c}}{\partial \hat{r}}\right|_{\hat{r}=0} = 0, \\ &\hat{c}|_{\theta=0} = \hat{c}|_{\theta=2\pi}, \quad \left.\frac{\partial \hat{c}}{\partial \hat{\theta}}\right|_{\theta=0} = \left.\frac{\partial \hat{c}}{\partial \hat{\theta}}\right|_{\theta=2\pi}, \end{aligned} \tag{10}$$

where $\hat{c}_i$ is the concentration of the nutrient at the pore inlet, pumped into the scaffold. Here, we propose that the nutrient consumption happens at the interface where cells interact with nutrient flow, i.e., the fluid–cell–layer interface. We further propose that the nutrient consumption is proportional to the nutrient concentration, with the coefficient being $\hat{\eta}$, which we call the "hunger rate," or heuristically, how fast the cells consume nutrient,[30–32] that is,

$$\hat{\boldsymbol{Q}}_{\boldsymbol{n}}\cdot\boldsymbol{n} = \hat{\eta}\hat{c}, \quad \text{at} \quad \hat{r} = \hat{a}. \tag{11}$$

C. Tissue growth

According to the experiments and observational facts,[8,33] cells proliferate more quickly when exposed to a more concentrated nutrient solution, higher shear stress at their surface and in regions where the pore configuration has higher curvature.[8,34] Therefore, we propose

$$\frac{\partial \hat{a}}{\partial \hat{t}} = -\hat{\lambda}\hat{c}\hat{\kappa}f(\hat{\sigma}_s). \tag{12}$$

Here, $\hat{\lambda}$ is the characteristic growth rate (mol^{-1} m^5 s^{-1}), $\hat{\kappa} = \hat{\mathbf{V}}\cdot\boldsymbol{n}$ is the mean curvature, and the function f captures the influence on tissue growth due to the total shear stress $\hat{\sigma}_s$, which will be defined later in more detail.

III. SCALING, NON-DIMENSIONALIZATION

To reduce the number of independent parameters, we non-dimensionalize the models for the (i) flow; (ii) nutrient concentration; and (iii) tissue growth described in Secs. II A–II C, respectively, using appropriate scaling factors introduced for each one below.

A. Fluid dynamics

We use the following scaling rules to non-dimensionalize the model given by (1)–(6):

$$\begin{aligned} \hat{\boldsymbol{u}} &= \frac{\hat{Q}_i}{\pi\hat{R}^2}\boldsymbol{u} = \frac{\hat{Q}_i}{\pi\hat{R}^2}(\epsilon u, \epsilon v, w), \\ (\hat{p}, \hat{\zeta}, \hat{\sigma}_s) &= \frac{\hat{\mu}\hat{L}\hat{Q}_i}{\pi\hat{R}^4}(p, \zeta, \sigma_s), \\ (\hat{r}, \hat{a}, \hat{z}) &= \hat{L}(\epsilon r, \epsilon a, z), \end{aligned} \tag{13}$$

where μ is the viscosity and $\hat{Q}_i$ is the inlet flux. $\hat{L}$ and $\hat{R}$ are the length and the typical pore radius, respectively. u, v, w, p, ζ, σ_s, r, a, and z are the corresponding dimensionless variables. From (1), the corresponding dimensionless equations governing the flow are given by

$$\frac{1}{\epsilon^2}\frac{\partial p}{\partial r} = \frac{1}{r}\frac{\partial}{\partial r}\left(r\frac{\partial u}{\partial r}\right) + \frac{1}{r^2}\frac{\partial^2 u}{\partial \theta^2} + \epsilon^2\frac{\partial^2 u}{\partial z^2} - \frac{u}{r^2} - \frac{2}{r^2}\frac{\partial v}{\partial \theta}, \tag{14}$$

$$\frac{1}{\epsilon^2 r}\frac{\partial p}{\partial \theta} = \frac{1}{r}\frac{\partial}{\partial r}\left(r\frac{\partial v}{\partial r}\right) + \frac{1}{r^2}\frac{\partial^2 v}{\partial \theta^2} + \epsilon^2\frac{\partial^2 v}{\partial z^2} - \frac{v}{r^2} + \frac{2}{r^2}\frac{\partial u}{\partial \theta}, \tag{15}$$

$$\frac{\partial p}{\partial z} = \frac{1}{r}\frac{\partial}{\partial r}\left(r\frac{\partial w}{\partial r}\right) + \frac{1}{r^2}\frac{\partial^2 w}{\partial \theta^2} + \epsilon^2\frac{\partial^2 w}{\partial z^2}, \tag{16}$$

$$\frac{1}{r}\frac{\partial}{\partial r}(ru) + \frac{1}{r}\frac{\partial v}{\partial \theta} + \frac{\partial w}{\partial z} = 0. \tag{17}$$

Substituting (13) into the dimensional boundary conditions given by (2) yields the dimensionless boundary conditions

$$u = v = w = 0 \quad \text{on} \quad r = a(\theta, z, t),$$
$$u = v = \frac{\partial w}{\partial r} = 0 \quad \text{at} \quad r = 0. \tag{18}$$

The dimensionless form of the constant fluid influx condition given by (3) is

$$\int_0^{2\pi} \int_0^a \sqrt{\epsilon^2 u^2 + \epsilon^2 v^2 + w^2}\, r\, \mathrm{d}r\, \mathrm{d}\theta = \pi. \tag{19}$$

Corresponding to (4), we assume that the dimensionless pressure drop across the length of the pore is given by $\zeta(t)$ (t is the dimensionless time and the scale will be introduced later in Sec. III C), a function monotonically increasing in t to keep the flux constant, as the pore shrinks due to cell proliferation. We therefore complete the system by applying the dimensionless boundary conditions

$$p|_{z=0} = \zeta(t), \quad p|_{z=1} = 0. \tag{20}$$

The dimensionless total shear stress at the channel walls, exerted by the nutrient flow, after manipulating (5), is given by

$$\sigma_s = \sqrt{|\boldsymbol{\sigma n}|^2 - ((\boldsymbol{\sigma n}) \cdot \boldsymbol{n})^2},$$
$$\boldsymbol{\sigma} = \begin{pmatrix} 2\epsilon \frac{\partial u}{\partial r} & \epsilon\left(\frac{1}{r}\frac{\partial u}{\partial \theta} - \frac{v}{r} + \frac{\partial v}{\partial r}\right) & \epsilon^2 \frac{\partial u}{\partial z} + \frac{\partial w}{\partial r} \\ \epsilon\left(\frac{1}{r}\frac{\partial u}{\partial \theta} - \frac{v}{r} + \frac{\partial v}{\partial r}\right) & 2\epsilon\left(\frac{1}{r}\frac{\partial v}{\partial \theta} + \frac{u}{r}\right) & \epsilon^2 \frac{\partial v}{\partial z} + \frac{1}{r}\frac{\partial w}{\partial \theta} \\ \epsilon^2 \frac{\partial u}{\partial z} + \frac{\partial w}{\partial r} & \epsilon^2 \frac{\partial v}{\partial z} + \frac{1}{r}\frac{\partial w}{\partial \theta} & 2\epsilon \frac{\partial w}{\partial z} \end{pmatrix}, \tag{21}$$

where the unit normal vector to the fluid–cell–layer interface, pointing inward in (6), is simplified as follows:

$$\boldsymbol{n} = \frac{\left(\boldsymbol{e}_r - \frac{1}{r}\frac{\partial a}{\partial \theta}\boldsymbol{e}_\theta - \epsilon \frac{\partial a}{\partial z}\boldsymbol{e}_z\right)}{\sqrt{1 + \frac{1}{r^2}\left(\frac{\partial a}{\partial \theta}\right)^2 + \epsilon^2 \left(\frac{\partial a}{\partial z}\right)^2}}. \tag{22}$$

B. Nutrient concentration

In order to non-dimensionalize the model given by (7)–(11) presented in Sec. II B, we use (13) along with a new scaling factor for the nutrient concentration as follows:

$$\hat{c} = \hat{c}_i c, \tag{23}$$

to arrive at

$$\frac{1}{\epsilon \mathrm{Pe}}\left[\frac{1}{r}\frac{\partial}{\partial r}\left(r\frac{\partial c}{\partial r}\right) + \frac{1}{r^2}\frac{\partial^2 c}{\partial \theta^2} + \epsilon^2 \frac{\partial^2 c}{\partial z^2}\right] = \frac{\partial c}{\partial r}u + \frac{1}{r}\frac{\partial c}{\partial \theta}v + \frac{\partial c}{\partial z}w,$$
$$\mathrm{Pe} = \frac{\epsilon \hat{L}\hat{Q}_i}{\pi \hat{R}^2 \hat{\Xi}}, \tag{24}$$

$$c|_{z=0} = 1, \quad \left.\frac{\partial c}{\partial r}\right|_{r=0} = 0,$$
$$c|_{\theta=0} = c|_{\theta=2\pi}, \quad \left.\frac{\partial c}{\partial \theta}\right|_{\theta=0} = \left.\frac{\partial c}{\partial \theta}\right|_{\theta=2\pi}, \tag{25}$$

$$\frac{1}{\epsilon \mathrm{Pe}}\left(\frac{\partial c}{\partial r}, \frac{1}{r}\frac{\partial c}{\partial \theta}, \epsilon \frac{\partial c}{\partial z}\right) \cdot \boldsymbol{n} = -\eta c, \quad \text{at} \quad r = a,$$
$$\eta = \frac{\pi \hat{R}^2 \hat{\eta}}{\epsilon \hat{Q}_i}, \tag{26}$$

where Pe and η are the Péclet number associated with the ratio of advective to diffusive transport rates of nutrients, and the dimensionless hunger rate, respectively. Note that, the timescale of cell proliferation is much longer compared to that of nutrient flow transport;[8,14] therefore, we employ the quasi-static assumption for (7) to obtain (24).

C. Tissue growth

Using the scaling relations given in (13) and (23) along with the additional scaling relations

$$\hat{t} = \frac{\hat{R}^2}{\hat{\lambda}\hat{c}_i} t, \quad \hat{\kappa} = \frac{1}{\hat{R}}\kappa, \tag{27}$$

for time and curvature, respectively, we can simplify (12) and find the dimensionless growth law as

$$\frac{\partial a}{\partial t} = -c\kappa f(\sigma_s). \tag{28}$$

Experimental data and analytical refrences[8,14] reveal that the functional form of f, introduced first in (12), can be interpreted as a piecewise constant function as shown in Fig. 2, which has a general form of

$$f(x) = F_1 + (F_2 - F_1)\left[\frac{1 + \tanh(m(x - \sigma_1))}{2}\right] - F_2\left[\frac{1 + \tanh(m(x - \sigma_2))}{2}\right]. \tag{29}$$

Here, $F_1 < F_2$, $\sigma_1 < \sigma_2$, $m \gg 1$ and based on the shear–stress scaling relation given in (13), σ_1 and σ_2 will typically be order-one quantities.[8,14] For large values of m, this corresponds to a function that has

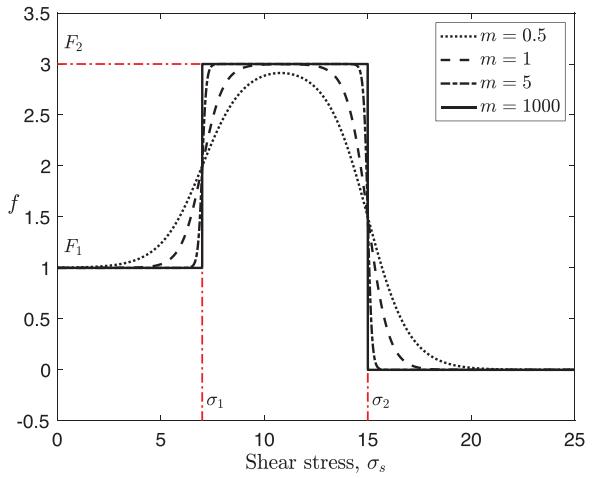

FIG. 2. The growth function f that appears in (28) and (29), with $F_1 = 1, F_2 = 3$, $\sigma_1 = 7$, and $\sigma_2 = 15$ for several values of m.

three regions in which it is approximately constant, connected by rapid but smooth transition regions.[8,14,26] According to (29) as well as Fig. 2, the tissue growth is low, enhanced, and zero when the total shear stress at the channel walls, exerted by the nutrient flow, is low, moderate, and high, respectively.

IV. ASYMPTOTIC ANALYSIS

The complete dimensionless system described in Sec. III is extremely hard to solve analytically, and it is also computationally costly to solve numerically by brute forces. Therefore, we make use of the fact that the pore aspect ratio $\epsilon = \hat{R}/\hat{L} \ll 1$. This allows us to achieve a simpler, computationally feasible, reduced asymptotic model. As stated earlier, we assume the initial fluid–cell–layer interface is sufficiently thin, so that it can be approximated by the underlying substrate geometry. Since the substrate is assumed to be roughly circular with small azimuthal and axial variation, we implement the relegation of spatial variations to first (axial) and second (azimuthal and axial) order in the aspect ratio ϵ.

We assume that the fluid–cell–layer interface is expressed as follows:

$$a(\theta, z, t) = a_0(t) + \epsilon a_1(z, t) + \epsilon^2 a_2(\theta, z, t) + \mathcal{O}(\epsilon^3), \tag{30}$$

where

$$a_2(\theta, z, t) = \Lambda_2(z, t)\cos(n\theta) + \Upsilon_2(z, t), \tag{31}$$

where $\Lambda_2(z,t)$ and $\Upsilon_2(z,t)$ are functions to be pinned down and n is an integer that describes the number of lobes in the geometry of the underlying substrate.[14] Although the above assumption poses constraints on the class of pores we can study, it is essential in attaining a balance between some level of generality and feasible asymptotic calculations. Here, the initial configuration of the fluid–cell–layer interface $a(\theta, z, 0)$ is given by the shape of the underlying substrate, and its subsequent evolution is described by the equation of cell growth given by (28). Below, we asymptotically expand the variables u, v, w, p, ζ, c, σ_s, f, and κ in the form of

$$x = x_0 + \epsilon x_1 + \epsilon^2 x_2 + \mathcal{O}(\epsilon^3), \tag{32}$$

where x is any variable listed above. With (30), the unit vector normal to fluid–cell–layer interface, pointing inward in (22) simplifies to

$$\boldsymbol{n} = \left(\boldsymbol{e}_r - \epsilon^2 \frac{1}{r}\frac{\partial a_2}{\partial \theta}\boldsymbol{e}_\theta - \epsilon^2 \frac{\partial a_1}{\partial z}\boldsymbol{e}_z\right)\Big|_{r=a_0} + \mathcal{O}(\epsilon^3). \tag{33}$$

A. Fluid dynamics

Assuming that the flow is independent of θ to leading order in ϵ, (14)–(21) along with the asymptotic expansions given by (32) yield the leading-order velocities u_0, v_0, w_0, pressure p_0, and pressure at the pore inlet ζ_0. Therefore, at $\mathcal{O}(1)$

$$\begin{gathered} u_0 = 0, \quad v_0 = 0, \quad w_0 = \frac{\zeta_0}{4}(a_0^2 - r^2), \\ p_0 = \zeta_0(1 - z), \quad \zeta_0 = \frac{8}{a_0^4}. \end{gathered} \tag{34}$$

Similarly, for $\mathcal{O}(\epsilon)$, we obtain

$$\begin{gathered} u_1 = \frac{\partial a_1}{\partial z}\frac{\zeta_0}{4a_0}\, r(a_0^2 - r^2), \quad v_1 = 0, \\ w_1 = \frac{a_1\zeta_0}{2a_0}(2r^2 - a_0^2), \end{gathered} \tag{35}$$

$$p_1 = -\frac{4\zeta_0}{a_0}\int_z^1 a_1(z', t)\,\mathrm{d}z', \quad \zeta_1 = -\frac{4\zeta_0}{a_0}\int_0^1 a_1(z, t)\,\mathrm{d}z. \tag{36}$$

Finally, for $\mathcal{O}(\epsilon^2)$

$$w_2 = \left[\frac{\Lambda_2}{2}a_0^{1-n}r^n\cos n\theta + \tilde{w}_2(r, z, t)\right]\zeta_0, \tag{37}$$

$$\frac{a_0^4}{4}p_2 = \left[3a_0^2\int_z^1 a_1^2(z', t)\,\mathrm{d}z' - a_0^3\int_z^1 \Upsilon_2(z', t)\,\mathrm{d}z' + \frac{1}{4}\int_z^1 a_1^4(z', t)\,\mathrm{d}z'\right]\zeta_0, \tag{38}$$

$$\zeta_2 = \frac{4}{a_0^4}\left[3a_0^2\int_0^1 a_1^2(z', t)\,\mathrm{d}z' - a_0^3\int_0^1 \Upsilon_2(z', t)\,\mathrm{d}z' + \frac{1}{4}\int_0^1 a_1^4(z', t)\,\mathrm{d}z'\right]\zeta_0, \tag{39}$$

$$\begin{aligned} w_2 = \Bigg[&\frac{\Lambda_2}{2}a_0^{1-n}r^n\cos n\theta + \frac{1}{a_0^4}\left(-3a_0^2a_1^2 + a_0^3\Upsilon_2 - \frac{a_1^4}{4}\right) \\ &\times\left(r^2 - a_0^2\right) - \frac{7}{4}a_1^2 + \frac{a_0\Upsilon_2}{2}\Bigg]\zeta_0. \end{aligned} \tag{40}$$

In addition, the dimensionless shear stress at the fluid–cell–layer interface is

$$\sigma_s = \sigma_{s_0} + \epsilon\sigma_{s_1} + \epsilon^2(\sigma_{s_{2a}}\cos n\theta + \sigma_{s_{2b}}) + \mathcal{O}(\epsilon^3), \tag{41}$$

where

$$\begin{gathered} \sigma_{s_0} = \frac{a_0}{2}\zeta_0, \quad \sigma_{s_1} = 2a_1\zeta_0, \\ \sigma_{s_{2a}} = \frac{n\Lambda_2\zeta_0}{2}, \quad \sigma_{s_{2b}} = \frac{1}{a_0^3}\left(-6a_0^2a_1^2 + 2a_0^3\Upsilon_2 - \frac{a_1^4}{2}\right)\zeta_0. \end{gathered} \tag{42}$$

Furthermore, the dimensionless curvature κ can be found as follows:

$$\begin{gathered} \kappa = \kappa_0(t) + \epsilon^2\kappa_2(z, t)\cos n\theta + \mathcal{O}(\epsilon^3), \\ \kappa_0 = \frac{1}{a_0}, \quad \kappa_2 = \frac{n^2\Lambda_2}{a_0^2}. \end{gathered} \tag{43}$$

B. Nutrient concentration

We substitute the asymptotic expansions given by (32) into (24)–(26) to retain the nutrient concentration at $\mathcal{O}(1)$, $\mathcal{O}(\epsilon)$, and $\mathcal{O}(\epsilon^2)$. Note that the Péclet number is defined as the ratio of advective to diffusive transport rates of nutrients. Here, we consider a distinguished limit of the nutrient Péclet number, which is $\mathrm{Pe} = \mathcal{O}(1)$. One may consider $\mathrm{Pe} = \mathcal{O}(\epsilon)$, if the main interest is on the effects of axial diffusion of the nutrient.[30–32] Our model can be readily extended to the general scenario. The dimensionless nutrient concentrations given by (24) at $\mathcal{O}\left(\frac{1}{\epsilon}\right)$, $\mathcal{O}(1)$, $\mathcal{O}(\epsilon)$, and $\mathcal{O}(\epsilon^2)$, respectively, simplify to the following expressions:

$$\frac{1}{\mathrm{Pe}}\left[\frac{1}{r}\frac{\partial}{\partial r}\left(r\frac{\partial c_0}{\partial r}\right) + \frac{1}{r^2}\frac{\partial^2 c_0}{\partial \theta^2}\right] = 0, \tag{44}$$

$$\frac{1}{\mathrm{Pe}}\left[\frac{1}{r}\frac{\partial}{\partial r}\left(r\frac{\partial c_1}{\partial r}\right)+\frac{1}{r^2}\frac{\partial^2 c_1}{\partial\theta^2}\right]=\frac{\partial c_0}{\partial r}u_0+\frac{1}{r}\frac{\partial c_0}{\partial\theta}v_0+\frac{\partial c_0}{\partial z}w_0, \quad (45)$$

$$\frac{1}{\mathrm{Pe}}\left[\frac{1}{r}\frac{\partial}{\partial r}\left(r\frac{\partial c_2}{\partial r}\right)+\frac{1}{r^2}\frac{\partial^2 c_2}{\partial\theta^2}+\frac{\partial^2 c_0}{\partial z^2}\right]=\frac{\partial c_0}{\partial r}u_1+\frac{\partial c_1}{\partial r}u_0+\frac{1}{r}\frac{\partial c_0}{\partial\theta}v_1+\frac{1}{r}\frac{\partial c_1}{\partial\theta}v_0+\frac{\partial c_0}{\partial z}w_1+\frac{\partial c_1}{\partial z}w_0, \quad (46)$$

$$\frac{1}{\mathrm{Pe}}\left[\frac{1}{r}\frac{\partial}{\partial r}\left(r\frac{\partial c_3}{\partial r}\right)+\frac{1}{r^2}\frac{\partial^2 c_3}{\partial\theta^2}+\frac{\partial^2 c_1}{\partial z^2}\right]=\frac{\partial c_0}{\partial r}u_2+\frac{\partial c_1}{\partial r}u_1+\frac{\partial c_2}{\partial r}u_0+\frac{1}{r}\frac{\partial c_0}{\partial\theta}v_2+\frac{1}{r}\frac{\partial c_1}{\partial\theta}v_1+\frac{1}{r}\frac{\partial c_2}{\partial\theta}v_0+\frac{\partial c_0}{\partial z}w_2+\frac{\partial c_1}{\partial z}w_1+\frac{\partial c_2}{\partial z}w_0. \quad (47)$$

The corresponding dimensionless boundary conditions given in (26) simplify to the following:

$$\frac{1}{\mathrm{Pe}}\frac{\partial c_0}{\partial r}=0, \quad \text{at} \quad r=a_0, \quad (48)$$

$$\frac{1}{\mathrm{Pe}}\frac{\partial c_1}{\partial r}=-\eta c_0, \quad \text{at} \quad r=a_0, \quad (49)$$

$$\frac{1}{\mathrm{Pe}}\left(\frac{\partial c_2}{\partial r}-\frac{1}{r^2}\frac{\partial a_2}{\partial\theta}\frac{\partial c_0}{\partial\theta}\right)=-\eta c_1, \quad \text{at} \quad r=a_0, \quad (50)$$

$$\frac{1}{\mathrm{Pe}}\left(\frac{\partial c_3}{\partial r}-\frac{1}{r^2}\frac{\partial a_2}{\partial\theta}\frac{\partial c_1}{\partial\theta}-\frac{\partial a_1}{\partial z}\frac{\partial c_0}{\partial z}\right)=-\eta c_2, \quad \text{at} \quad r=a_0, \quad (51)$$

by using (33).

1. Leading-order analysis

From (44) and (48), we obtain $\frac{\partial c_0}{\partial r}=0$, hence c_0 is a function of z only. Using (34) in (45) yields

$$\frac{1}{\mathrm{Pe}}\left[\frac{1}{r}\frac{\partial}{\partial r}\left(r\frac{\partial c_1}{\partial r}\right)+\frac{1}{r^2}\frac{\partial^2 c_1}{\partial\theta^2}\right]=\frac{\partial c_0}{\partial z}\frac{\zeta_0}{4}(a_0^2-r^2). \quad (52)$$

Next, we integrate (52) over the pore cross section by applying $\int_0^{2\pi}\int_0^{a_0}\cdot r\,dr\,d\theta$ operator, along with (25), to obtain

$$\frac{\partial c_0}{\partial z}=-2\eta a_0 c_0, \quad (53)$$

and together with the condition that $c_0|_{z=0}=1$ [see (25)], we arrive at

$$c_0(z)=e^{-2\eta a_0 z}. \quad (54)$$

2. First-order analysis

We use (34), (35), and (54) to simplify (46) and then integrate over the pore cross section and apply (25) to obtain

$$\frac{1}{\mathrm{Pe}}\left[a_0\frac{\partial c_2}{\partial r}\Big|_{r=a_0}+\frac{1}{2}a_0^2\frac{\partial^2 c_0}{\partial z^2}\right]=\frac{\zeta_0 a_0^4}{16}\frac{\partial c_1}{\partial z}. \quad (55)$$

Simplifying (50) by (54) and then plugging into (55) gives

$$\frac{\partial c_1}{\partial z}+2a_0\eta c_1=\frac{4a_0^4}{\mathrm{Pe}}\eta^2 e^{-2\eta a_0 z}, \quad (56)$$

which is solved [by using the initial condition $c_1|_{z=0}=0$ given in (25)],

$$c_1(z)=\frac{4a_0^4}{\mathrm{Pe}}\eta^2 z e^{-2a_0\eta z}. \quad (57)$$

3. Second-order analysis

Similarly, we plug in (34), (35), and (40) into (47) and (51) to obtain

$$\frac{1}{\mathrm{Pe}}\left[a_0\frac{\partial c_3}{\partial r}\Big|_{r=a_0}+\frac{1}{2}a_0^2\frac{\partial^2 c_1}{\partial z^2}\right]=\frac{\zeta_0(-2a_0^2a_1^2+a_1^4)}{16}\frac{\partial c_0}{\partial z}+\frac{\zeta_0 a_0^4}{16}\frac{\partial c_2}{\partial z}, \quad (58)$$

$$\frac{1}{\mathrm{Pe}}\frac{\partial c_3}{\partial r}\Big|_{r=a_0}-\frac{1}{\mathrm{Pe}}\frac{\partial a_1}{\partial z}\frac{\partial c_0}{\partial z}=-\eta c_2. \quad (59)$$

Combining (58) and (59), with some manipulations and using (54), (57), and $c_2|_{z=0}=0$ [see (25)], gives

$$c_2(z)=e^{-2a_0\eta z}\left[-\frac{4\eta a_0^2(a_1-a_1|_{z=0})}{\mathrm{Pe}}-\frac{16a_0^7\eta^3}{\mathrm{Pe}^2}z+\frac{8a_0^8\eta^4}{\mathrm{Pe}^2}z^2-2\eta\int_0^z\left(\frac{2a_1^2}{a_0}-\frac{a_1^4}{a_0^3}\right)dz'\right]. \quad (60)$$

C. Tissue growth

We simplify (28) using (30), (42), and (43) along with Taylor expansion of f [given in (29)] to obtain

$$\frac{\partial a_0}{\partial t}=-c_0\kappa_0 f, \quad (61)$$

$$\frac{\partial a_1}{\partial t}=-c_0\kappa_0\sigma_{s_1}f'-c_1\kappa_0 f, \quad (62)$$

$$\frac{\partial \Lambda_2}{\partial t}=-c_0\kappa_2 f-c_0\kappa_0\sigma_{s_{2a}}f', \quad (63)$$

$$\frac{\partial \Upsilon_2}{\partial t}=-c_2\kappa_0 f-c_1\kappa_0\sigma_{s_1}f'-c_0\kappa_0\left(\sigma_{s_{2b}}f'+\frac{1}{2}\sigma_{s_1}^2 f''\right). \quad (64)$$

Here, f, f', f'' are all evaluated at σ_{s_0} and the initial values for a_0, a_1, Λ_2, and Υ_2 are prescribed. Note that f, κ_0, κ_2, c_0, c_1, and c_2 are given in (29), (43), (54), (57), and (60), respectively.

V. RESULTS

In this section, we present and analyze simulations of the models given by (29), (43), (54), (57), (60), (61)–(64). Our numerical scheme is straightforward, based on implicit time-stepping of fluid–cell–layer interface evolution [i.e., (61)–(64)], and trapezoidal quadrature to evaluate the integrals in (60). To fully specify our model, various dimensional and dimensionless parameters given in Tables I and II, respectively, are estimated based on the typical ranges arising in tissue engineering applications,[8,14,32,35–37] specifically, the dimensionless parameter Péclet number Pe and hunger rate η, which show the ratio of advective to diffusive transport rates of nutrients and how fast the cells consume the nutrients, respectively. Their values vary for different nutrients and cells, respectively, and

TABLE I. Dimensional parameter values[8,14,32,35–37] for the model.

Parameter	Description	Typical value
$\hat{Q}_i$	Inlet flux	1 μl/min
$\hat{R}$	Fluid–cell–layer interface radius	400 μm
$\hat{L}$	Fluid–cell–layer interface length	2 mm
$\hat{c}_i$	Nutrient concentration at the pore inlet	1–10 mol/m^3
$\hat{\Xi}$	Diffusion coefficient of nutrient	$10^{-8} - 10^{-6}$ m^2/s
$\hat{\eta}$	Hunger rate	$0 - 10^{-4}$ m/s

TABLE II. Dimensionless parameter values[8,14,32,35–37] for the model.

Parameter	Formula	Typical value
ϵ	$\hat{R}/\hat{L}$	0.2
Pe	$(\epsilon\hat{L}\hat{Q}_i)/(\pi\hat{R}^2\hat{\Xi})$	$1 - 10$
η	$(\pi\hat{R}^2\hat{\eta})/(\epsilon\hat{Q}_i)$	$0 - 0.25$

$\mathrm{Pe} = 1 - 10$, $\eta = 0 - 0.25$, and $\epsilon = 0.2$ are chosen in all simulations (see Table II).

A. Incubation simulation

Figure 3 shows the shape of the fluid–cell–layer interface at different times for several values of hunger rate $\eta = 0$, 0.05, and 0.1 in panels (a), (b), and (c), respectively [see Fig. 3(d), Multimedia view]. The initial geometry of the pore is wider on the top and narrower at the bottom with $a_0(0) = 0.9$, $a_1(z,0) = -z - 0.5$, $\Lambda_2(z,0) = -z + 2$, $\Upsilon_2(z,0) = -z + 2$ and $n = 4$. Note that, with this chosen initial pore profile, we are able to compare our results with the ones from Sanaei *et al.*,[14] when the hunger rate is set to be zero. However, our model is capable of generating results for any initial pore profile. Note that the color map for the surface plots shows the nutrient concentration within the channel, which will be explained in detail in Fig. 5. At $t = 0$, when the pore is at its initial configuration, cells with negligible thickness are attached to the pore wall; therefore, $a(\theta, z, t)$ should be regarded as the initial shape of the pore. As nutrients pass through the pore, cells consume the nutrients and proliferate, gradually filling the space within the pore, which can be observed from the shrinkage of the fluid–cell–layer as time passes [$a(\theta, z, t)$ is decreasing in t]. This can be seen as the fluid–cell–layer shrinks more as time passes. The dimensionless final time $t_f = 0.25$ is chosen to be sufficiently large so that the incubation process has terminated for all the cases shown in the figure.

Another important observation is the "sequential eating" phenomena of cells in the pore. Our results show that the larger the hunger rate is, the longer time it takes for the incubation process to terminate. This can be explained as below. Given a fixed nutrient supply, when hunger rate is large, initially a larger portion of the nutrient is consumed by cells at the top, so very little is left for cells at the bottom. Recall that cells at the top of the pore stop to proliferate as the shear stress increases beyond its threshold σ_2 [see (28) and (29)]. As consumption by cells at the top decreases, more nutrient is left for cells at the bottom. This demonstrates the "sequential eating" phenomenon, which also appears in experimental observations.[20] On the other hand, when $\eta = 0$, the concentration is held constant across the pore, so cells at different depths of the pore are exposed to the same amount of nutrient. Thus, cells will proliferate simultaneously. The larger the hunger rate, the more the "sequential eating" phenomenon will be, and therefore it takes longer for the system to terminate and reach the steady state (no proliferation happens). Such observations can be more vividly seen in Fig. 3(d) (Multimedia view).

Figures 4(a) and 4(b) show the cross section of scaffold pore at the initial and final (t_f) times of the tissue growth process, respectively, for two values of hunger rate $\eta = 0$ and 0.1 with the initial pore radius as in Fig. 3. As observed, the tissue will grow so that ultimately the tube is circular in cross section, but the radius may vary along the axis, depending on the initial tube geometry and the hunger rate. These two figures are consistent with the results at $t = 0.25$ shown in Figs. 3(a)–3(c). Figures 4(c)–4(f) compare the radii of the fluid–cell–layer interface of the model we propose in this paper with those of the model developed in Sanaei *et al.*[14] (see $\eta = 0$ curves). The leading order of the radius of the fluid–cell–layer interface a_0 varies at different z levels when $\eta = 0.1$, but with $\eta = 0$, a_0 is of the same value throughout the scaffold pore. This is also observed in a_1 and Υ_2. The difference in radii with respect to z for a non-zero value of η causes difference in the shear stress and as a consequence affects the amount of tissue growth in the tube. On the other hand, Λ_2 varies along the tube axis for both hunger rate values. Figures 4(g) and 4(h) show that the leading order of the shear stress σ_{s_0} varies with z, when $\eta = 0.1$ and the first order of the shear stress σ_{s_1} takes longer time to reach a steady state compared to the scenario when $\eta = 0$. One can easily check that, for other initial conditions prescribed in Sanaei *et al.*,[14] our model yields the same results when hunger rate η is set to be zero, which is equivalent to assuming that no nutrient depletion happens in the model. Hence, our model is compatible with the models proposed in previous literature,[14,26,34] and provides more insight on the reality when nutrient concentration is not constant throughout the scaffold pores.

B. Nutrient consumption and "hunger rate"

There are several noticeable differences when the nutrient concentration depletion is taken into consideration. As mentioned before, $\eta = 0$ corresponds to the assumption that nutrient supply is in excess, so the nutrient concentration is held at constant across the pore axis. As expected, a_0 is uniform at different heights of the pore [see Fig. 4(c), the black curves at different heights collapse to the red curve at $z = 0$]. The red curves in Fig. 4(b) show that when nutrient consumption is considered, a is smaller for larger values of z, indicating that there is more tissue growth at the bottom part of the pore. This can be explained by the fact that the shear stress dominant term σ_{s_0} in Fig. 4(g) grows more slowly when $\eta = 0.1$ compared to $\eta = 0$. As a result, the shear stress would increase more slowly in the former case, and due to the bell shape of f (see Fig. 2), cells in the former case will experience a longer period of growth, which can be seen in Fig. 4(c) (takes longer time for a_0 to reach the steady state phase). In addition, the curves for σ_{s_1} with $\eta = 0.1$ in Fig. 4(h) also reveal a delayed change compared to the case when $\eta = 0$.

Evidently, the most dominant consequence of cells' nutrient consumption is the change in nutrient concentration across the pore. In Fig. 5, we compare the nutrient concentration $c = c_0 + \mathcal{O}(\epsilon)$ [see (54) for c_0] for two choices of two hunger rates, $\eta = 0.05$ and 0.10.

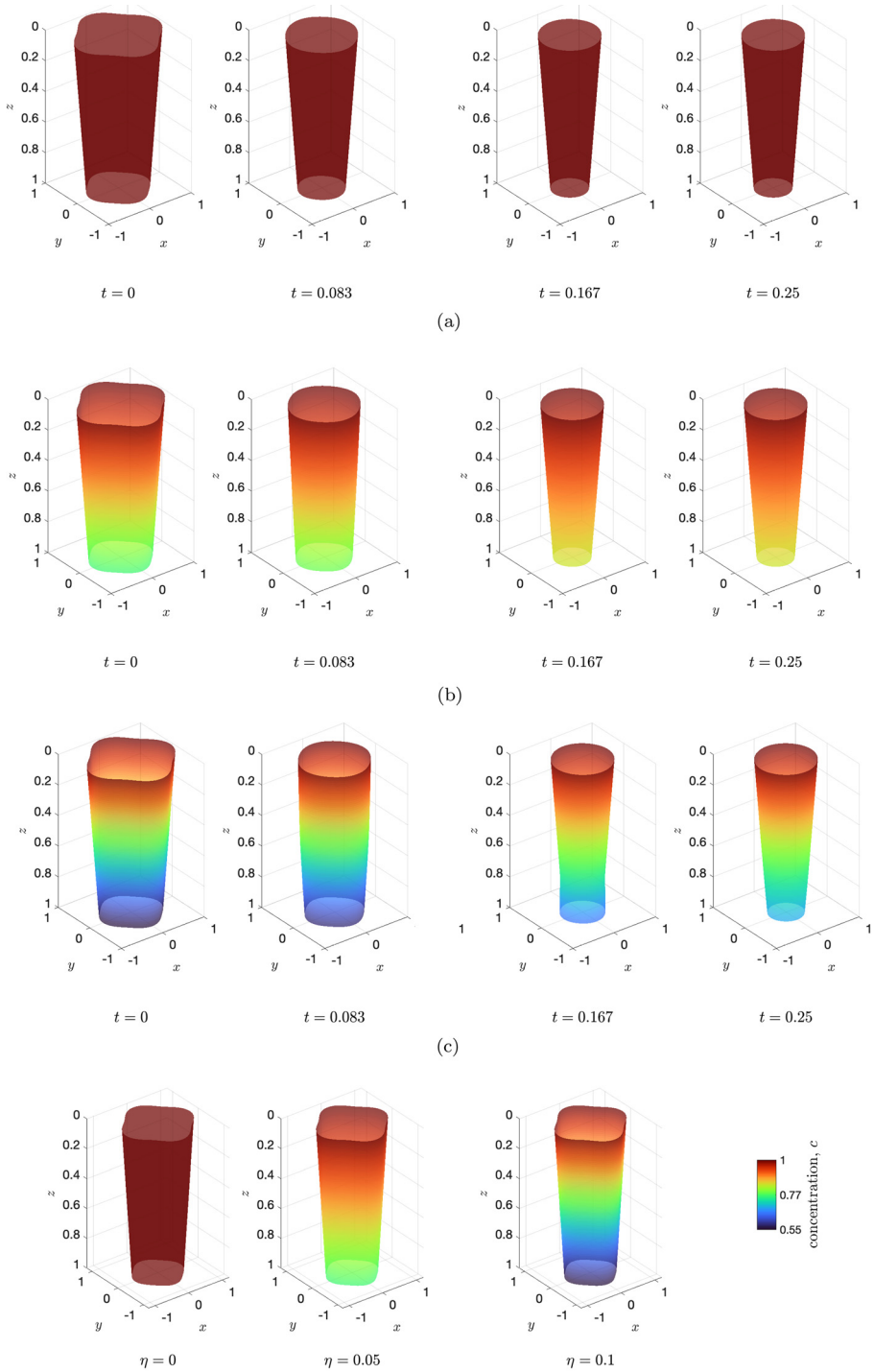

FIG. 3. [(a)–(c)] Fluid–cell–layer interface $a(\theta, z, t) = a_0(t) + \epsilon a_1(z, t) + \epsilon^2(\Lambda_2(z, t)\cos(n\theta) + \Upsilon_2(z, t)) + O(\epsilon^3)$, at different times with hunger rates $\eta = 0$, 0.05 and 0.1, respectively. Here, $a_0(0) = 0.9$, $a_1(z, 0) = -z - 0.5$, $\Lambda_2(z, 0) = -z + 2$, $\Upsilon_2(z, 0) = -z + 2$, $n = 4$, $\epsilon = 0.2$ and $Pe = 1$. f is defined and graphed in (29) and Fig. 2, respectively, with $m \to \infty$. The color bar shows the nutrient concentration. (d) Provides more details on the pore evolution. Multimedia view: https://doi.org/10.1063/5.0071171.1

Figures 5(a) and 5(b) show that, regardless of time t and depth z chosen, the concentration associated with the case $\eta = 0.05$ is always larger than that associated with $\eta = 0.10$. This can be primarily attributed to the leading term of concentration c_0. In Figs. 5(c) and 5(d), we observe that throughout the simulation, c_0 and c_1 are lower when η is higher, regardless of the time t and depth z. Note that the dynamics in concentration c to the leading order is captured by the leading term c_0. Hence, it can be concluded that cells with a larger "hunger rate" η tend

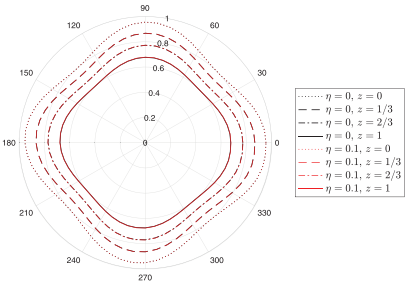

(a) $t = 0$

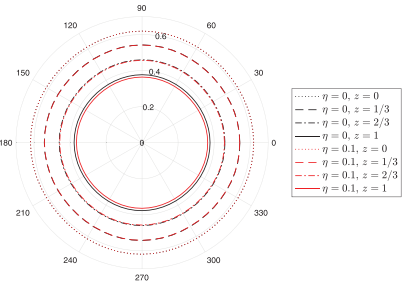

(b) $t = t_f$

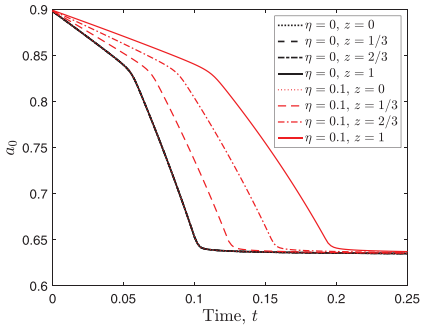

(c)

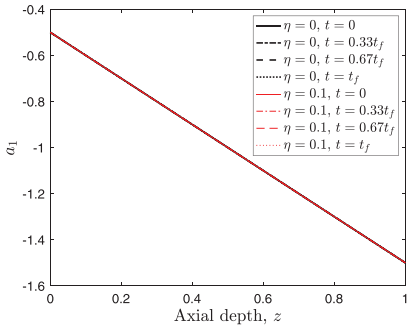

(d)

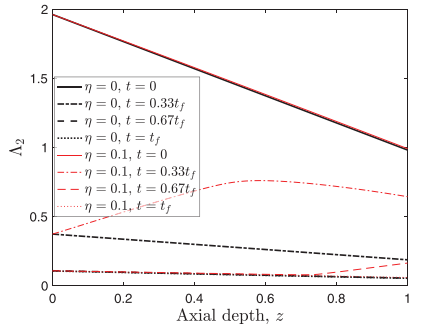

(e)

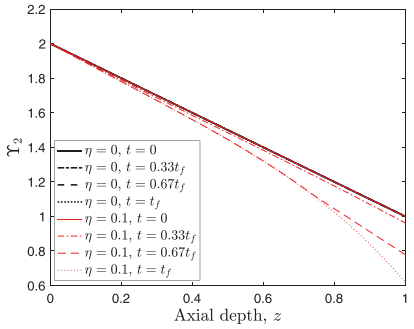

(f)

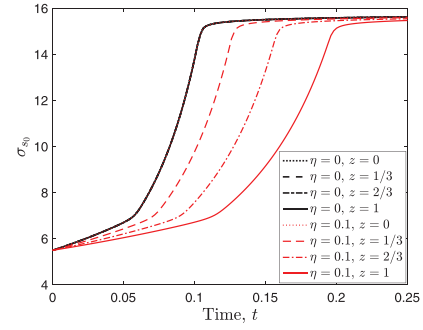

(g)

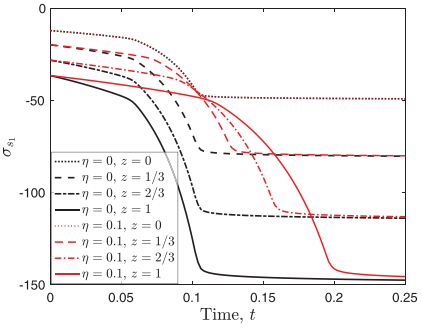

(h)

FIG. 4. [(a) and (b)] Fluid–cell–layer interface $a(\theta, z, t) = a_0(t) + \epsilon a_1(z, t) + \epsilon^2(\Lambda_2(z,t)\cos(n\theta) + \Upsilon_2(z,t)) + O(\epsilon^3)$ at the initial and final (tf) time, respectively. (c)–(f) are profiles for a0, a1, Λ_2 and Υ_2, respectively. (g) and (h) are σ_{s_0} and σ_{s_1} vs time, respectively. All graphs are for $\eta = 0$ and $\eta = 0.1$ as well as several different times and z. Here, $a_0(0) = 0.9$, $a_1(z,0) = -z - 0.5$, $\Lambda_2(z,0) = -z + 2$, $\Upsilon_2(z,0) = -z + 2$, $n = 4$, $\epsilon = 0.2$ and Pe = 1. f is defined and graphed in (29) and Fig. 2, respectively, with $m \to \infty$.

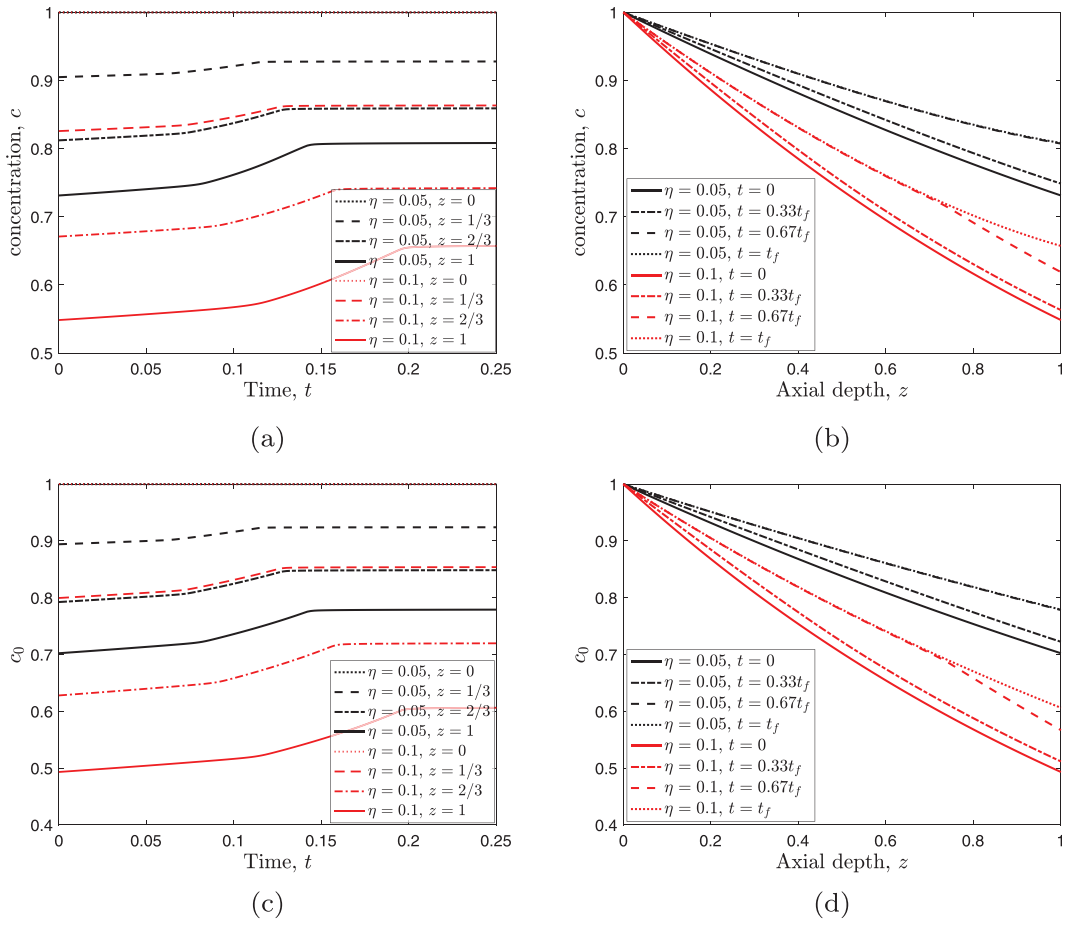

FIG. 5. [(a) and (b)] Nutrient concentration profile c; [(c) and (d)] leading-order nutrient concentration profile c_0 vs t and z for $\eta = 0.05$ and 0.1. Here, $a_0(0) = 0.9$, $a_1(z,0) = -z - 0.5$, $\Lambda_2(z,0) = -z + 2$, $\Upsilon_2(z,0) = -z + 2$, n = 4, $\epsilon = 0.2$ and Pe = 1. f is defined and graphed in (29) and Fig. 2, respectively, with $m \to \infty$.

to "eat more," resulting in a lower nutrient concentration in the pore. Note that, depending on the cells and their properties, the hunger rate would vary. In reality, experimentalists make sure that there is always enough nutrients within the scaffold channels for the cells to proliferate, otherwise they may die or be damaged. Therefore, what is important in experiments is that the inlet flux of nutrients $\hat{Q}_i$ would be large enough such that autologous cell sources, seeded within the tissue engineering scaffold, proliferate as the nutrient-rich culture medium flows through the scaffold.[8,14] In other words, the value of the dimensionless hunger rate $\eta = (\pi \hat{R}^2 \hat{\eta})/(\epsilon \hat{Q}_i)$ could be adjusted with the inlet flux of nutrients in order to provide appropriate environment for the cells to incubate. Therefore, the value of nutrient concentration should not get close to zero within the scaffold channel.

In addition to consuming more nutrients, cells with larger η also "eat faster." In Fig. 5(b), the concentration c associated with $\eta = 0.10$ decreases more rapidly with respect to z compared to the case when $\eta = 0.05$. Since the nutrient flows into the pore from $z = 0$, it illustrates that the consumption of nutrient by cells residing on the top part of the pore leads to an obvious decrease in nutrient concentration there. As time goes, however, the nutrient concentration decreases less rapidly. The reasoning based on intuition is that the cells residing on the top part in the scaffold have stopped growing; therefore, they do not consume the nutrient anymore. They take the "best" position to consume the nutrient, so they grow quickly and the radii of the fluid–cell–layer have shrunk small enough so that the shear stress $\sigma_{s_0} > \sigma_2$. Then, according to (28) and (29) the cell proliferation stops. At a specific depth z_0, as cells above gradually stop growing, less nutrient is being consumed and, hence, the concentration at this depth $c(z = z_0, t)$ increases with respect to t. Finally, when all cells above z_0 stop growing, $c(z = z_0, t)$ becomes constant, as is evident in Fig. 6. The time at which cells above z_0 stop growing is demonstrated by the turning point where the average radius of the fluid–cell interface defined as $\bar{a}(z_0, t) = \frac{1}{2\pi}\int_0^{2\pi} a(z_0, t, \theta)\, d\theta$ stops to decrease and becomes flat. The average is introduced here because a shows azimuthal variation with respect to θ.

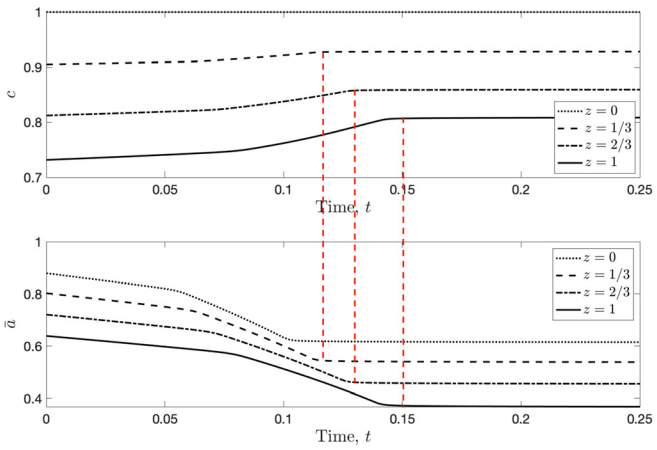

FIG. 6. Nutrient concentration and averaged radius of fluid–cell–layer interface defined as $\bar{a}(z,t) = \frac{1}{2\pi}\int_0^{2\pi} a(z,t,\theta)\,\mathrm{d}\theta$ vs time at several z for $\eta = 0.05$. Here, $a_0(0) = 0.9$, $a_1(z,0) = -z - 0.5$, $\Lambda_2(z,0) = -z + 2$, $\Upsilon_2(z,0) = -z + 2$, $n = 4$, $\epsilon = 0.2$ and $\mathrm{Pe} = 1$. f is defined and graphed in (29) and Fig. 2, respectively, with $m \to \infty$. The vertical red dotted lines are added to guide the eyes.

C. Total tissue growth

We define the total tissue growth $V(t)$ to be the total volume of the tissue growth within the pore at time t, i.e.,

$$V(t) = \int_0^1 \int_0^{2\pi} \int_{a(\theta,z,t)}^{a(\theta,z,0)} r\,\mathrm{d}r\,\mathrm{d}\theta\,\mathrm{d}z = \int_0^1 \int_0^{2\pi} \frac{1}{2}(a^2(\theta,z,0) - a^2(\theta,z,t))\mathrm{d}\theta\,\mathrm{d}z. \tag{65}$$

Figures 7(a) and 7(b) show the total dimensionless tissue growth $V(t)$ vs time t, for several different values of hunger rate η and the number of corners n, respectively. In Sec. V B, we have already mentioned that a larger hunger rate η implies a longer incubation process and the same conclusion can be observed in Fig. 7(a). The incubation terminates when the curve for $V(t)$ becomes flat. Notice that when $\eta = 0.1$, this happens at around $t = 0.2$, and when $\eta = 0.01$ this happens at around $t = 0.1$.

Recall that in Sec. V A, we discussed the phenomenon of "sequential eating." A smaller η (or even $\eta = 0$) implies less sequential but more simultaneous proliferation. Correspondingly, one also observes that the slope of the total tissue growth curve $V(t)$, which reflects how fast the total tissue growth is accumulating, is smaller when η is higher, since simultaneous proliferation of all cells (when η is smaller) yields faster tissue growth than sequential proliferation (when η is larger).[20] Observe that, albeit tiny, the larger the hunger rate, the more total tissue growth the system can accumulate as shown in Fig. 7(a). This is straightforward to understand: as stated above, when η is larger, it takes longer time for the system to terminate. So the total supply, and hence the total consumption, of nutrients is higher, yielding more tissue growth. We can conclude that cells with high hunger rate would only yield marginal increase in the total tissue growth.

Furthermore, in the work by Sanaei *et al.*[14] (or equivalently, when $\eta = 0$ in our work), the total tissue growth is piece-wise linear. This occurs due to the piece-wise form of f [see (29)], when the shear stress reaches its threshold levels σ_1 and σ_2. In the case when $\eta = 0$, cells at different tube depths experience a change in the value of the growth function f simultaneously; so, the piece-wise linearity of f is preserved and inherited in the total tissue growth. In contrast for $\eta > 0$, we see a more smooth total tissue curve, representing a more natural transition process. The growth rate is not uniform along the tube depth. The top cells proliferate first, the bottom cells then follow [as is evident in Fig. 3(d), Multimedia view]. Our model is seen to "smooth out" the original total tissue growth curve, capturing the transition process, which is also introduced in Fig. 7(a).

Another observation is that n rarely influences the simulation results. In Fig. 7(b), we see that for different values of n (the number of lobes, which we take as a proxy for the shape of the underlying scaffold

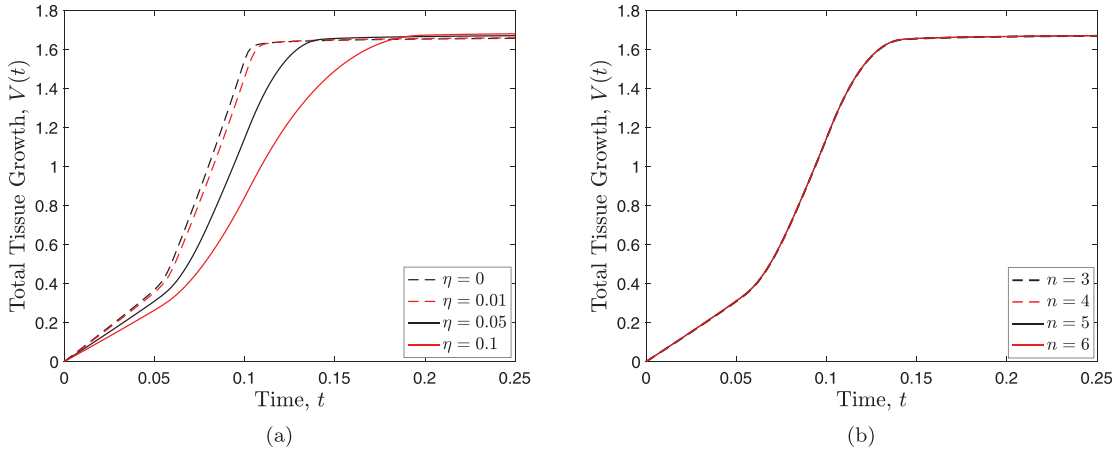

FIG. 7. (a) Total tissue growth V(t) vs time t for several values of hunger rate η. Total tissue growth is defined as $V(t) = \int_0^1 \int_0^{2\pi} \frac{1}{2}(a^2(\theta,z,0) - a^2(\theta,z,t))\mathrm{d}\theta\,\mathrm{d}z$, or heuristically, the total volume occupied by tissue. Here, $a_0(0) = 0.9$, $a_1(z,0) = -z - 0.5$, $\Lambda_2(z,0) = -z + 2$, $\Upsilon_2(z,0) = -z + 2$, $n = 4$, $\epsilon = 0.2$, and $\mathrm{Pe} = 1$. f is defined and graphed in (29) and Fig. 2, respectively, with $m \to \infty$. (b) Total tissue growth vs time for different n with $\eta = 0.05$. Other parameters and initial conditions are chosen to be the same as in (a).

pore),[14] the total tissue growth would remain the same as the proliferation terminates. Moreover, since the curves corresponding to different n collapse to exactly one curve, this also indicates that the rate of tissue accumulation would be the same for different n throughout the whole process. This observation is compatible with the one in the work by Sanaei *et al.*,[14] which reports that n does not influence the total tissue growth without the dimension of concentration c. Therefore, the conclusion is the same when concentration is added.

D. Scaffold design with respect to the final pore geometry

In a laboratory environment, researchers sometimes prescribe the final geometry of the desired tissue growth, and try to figure out an initial pore configuration so that the goal can be targeted. Our model provides a convenient guidance to how the pore should be designed, given the targeting tissue geometry. In this section, we propose an algorithm that can guide the pore design, and demonstrate how it can be used through several examples. Note that, the full advection–diffusion equation is a parabolic equation; therefore, it is not reversible in time, but under quasi-static assumption, our system is time reversible.[32,38,39] Observe that the fluid dynamics for nutrient flow would be the same in both the original and the reverse directions; hence, the only part that shall be modified is the tissue growth. Instead of tissue proliferation, now the tissue would be shrinking, i.e.,

$$\frac{\partial a}{\partial t} = +c\kappa f(\sigma_s) \tag{66}$$

in dimensionless form and in contrast to (28).

Though one may want different radii for the final geometry, after the parameters related to cell growth are prescribed, the final radius must fall in some feasible range, for if the radius is too small, shear stress would be too large to support cell growth, as shown in the tail part of Fig. 2. Recall from (34) and (42) that $\sigma_{s_0} = 4/a_0^3$. As $f(\sigma_s) = 0$ for $\sigma_s > \sigma_2$, in order for cells to grow, we must require $\sigma_{s_0} \leq \sigma_2$, otherwise the initial shear stress would be too large to support tissue growth. Therefore, the smallest possible final radius, which also corresponds to the largest possible volume of tissue growth, is precisely achieved when $a_0 \geq (4/\sigma_2)^{(1/3)}$.

It is efficient to have a scaffold pore structure resulting in a uniform final pore profile, meaning that most of the tube is being used for the cells to proliferate. As a demonstration, we solve (66) for the initial scaffold pore design when the final geometry is uniform. As shown in Figs. 8(a) and 8(b) [see also Fig. 8(c), Multimedia view], we prescribe the final geometry, and run the algorithm to figure out the initial pore design, specifying different number of corners. The algorithm terminates when the pore radius does not increase. The uniformly circular black curves show the prescribed final geometry, and the red curves show the initial pore design calculated by our algorithm. We can see from the figure that when n is small, or with few corners, we can afford to have an initial pore design with larger radius. Therefore, more total tissue growth is generated when n is smaller; in other words, with more corners, we get a smaller initial pore design and less total tissue growth.

Another observation is that, to sustain a uniform final geometry, the initial pore must be designed in a funnel-like shape. The designed pore should be wider at the top of the tube at $z = 0$ and gradually become thinner toward the bottom at $z = 1$. Since the concentration is higher at the top, cell growth is faster at the top; therefore to achieve uniform final geometry, larger space is needed at the top to accommodate more tissue growth. This can be seen from Fig. 8(a) that in each graph, the dotted red curve, which corresponds to the initial pore design at the top of the tube, is wider than the solid red curve, which corresponds to the initial pore design at the bottom. Note that, similar to Fig. 3, the color map for the surface plots in Fig. 8(c) shows the nutrient concentration within the channel.

VI. CONCLUSION

As a broad continuation of the model proposed by Sanaei *et al.*,[14] we present a more comprehensive and realistic mathematical model by including the fluctuation of nutrient concentration during proliferation. The flow of nutrients is captured by the Stokes equation, with no-slip and no-penetration boundary conditions at the channel wall. The concentration of the flow is governed by the advection–diffusion equation for nutrient flux, with the effects of nutrient diffusion and fluid drift as a consequence of the flow interacting with pore wall, while the boundary condition of nutrient flux also depends on the "hunger rate" of the cells. Cell proliferation is modeled based on the nutrient concentration, curvature of cell–layer interface, as well as biological cell growth rule under fluid shear stress. The resulting equations are analyzed using asymptotic analysis [based on the small aspect ratio of the pore as well as the expression for the fluid–cell–layer interface given in (30) and (31)], where we are able to determine the dominant equations for nutrient concentration. With the assumption that tissue growth happens on a much longer timescale than that associated with transport of fluid through the pore, we adopt the quasi-static assumption and update the rate of tissue growth based on the nutrient concentration. The numerical simulation results from our extended model are compared with those from Sanaei *et al.*,[14] which assumes the nutrient concentration is always constant along the pore depth. Our results also demonstrate consistency with the experimental result from Rumpler *et al.*[8] as also reported in Ref. 14.

Innovatively, our model includes a parameter representing the rates of nutrient consumption of different cells. Our results show that a larger "hunger rate" $\hat{\eta}$, or in its dimensionless form η, yields longer incubation time, lower nutrient concentration, different final pore geometries, and more total tissue growth. Albeit the changes in the final pore geometry are rather small, the processes during which final geometries are achieved are noticeably different. With a higher hunger rate, the pore geometry changes "sequentially" from top to bottom as time passes. With a lower or even zero hunger rate (representing almost excess or excess nutrient supply), the top part and bottom part of the pore react almost simultaneously, without the sequential behavior. Furthermore, we present a corresponding reverse algorithm, which, given the targeting final pore geometry, can yield feasible initial scaffold pore designs. One simple example is discussed in this paper, but the algorithm can be practically applied to any final pore geometry to design an appropriate initial scaffold pore geometry.

Finally, in terms of future improvements, our model considers the homogeneous properties of cells while neglecting the possible variants such as a changeable "hunger rate" when the environment varies.[20] Additionally, in this work, we do not consider scaffold deformations. In

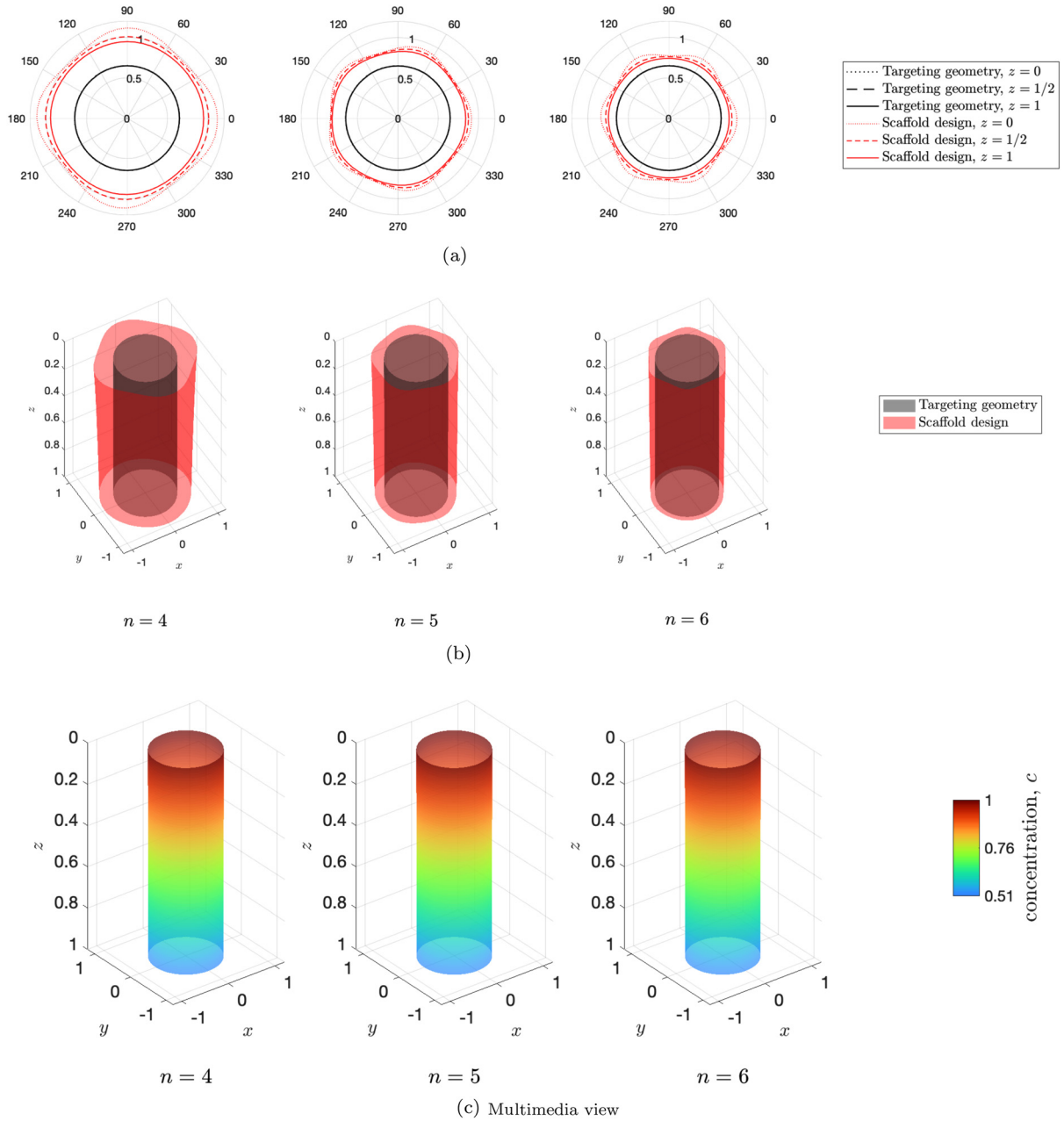

FIG. 8. (a) Channel cross section and (b) surface plots, respectively, for the scaffold design with uniform final radius $a(\theta, z, t_f) = 0.6$ for different values of the number of lobes n. Here, $\epsilon = 0.2$, Pe $= 1$, $\eta = 0.1$, and f is defined and graphed in (29) and Fig. 2, respectively, with $m \to \infty$. (c) More details on the reverse algorithm. The color bar shows the nutrient concentration. Multimedia view: https://doi.org/10.1063/5.0071171.2

reality, however, tissue is cultured in an elastic scaffold design. The tissue growth and shear stress may cause a slight deformation of the scaffold, thus affecting the overall growth process.[16,25,40–43] Nevertheless, our model and algorithm are practical and computationally efficient, providing a convenient tool to simulate tissue growth results and propose a scaffold design given the desired tissue model outcome.[44]

ACKNOWLEDGMENTS

The authors gratefully acknowledge support from the following sources: Z.Z. and X.L. from the Summer Undergraduate Research Experience offered by Courant Institute, New York University; P.S. from the National Science Foundation (NSF) under

Grant Nos. RTG/DMS-1646339 and DMS-2108161 as well as an Institutional Support of Research and Creativity (ISRC) grant provided by New York Institute of Technology. The authors thank C. Peskin for useful discussions.

AUTHOR DECLARATIONS

Conflict of Interest

The authors have no conflict of interest to disclose.

Author Contributions

Z.Z. and X.L. contributed equally to this work.

DATA AVAILABILITY

The data that support the findings of this study are available from the corresponding author upon reasonable request.

REFERENCES

[1]F. R. Rose and R. O. Oreffo, "Bone tissue engineering: Hope vs hype," Biochem. Biophys. Res. Commun. **292**, 1–7 (2002).
[2]I. Martin, D. Wendt, and M. Heberer, "The role of bioreactors in tissue engineering," TRENDS Biotechnol. **22**, 80–86 (2004).
[3]M. Paris, A. Götz, I. Hettrich, C. M. Bidan, J. W. Dunlop, H. Razi, I. Zizak, D. W. Hutmacher, P. Fratzl, G. N. Duda *et al.*, "Scaffold curvature-mediated novel biomineralization process originates a continuous soft tissue-to-bone interface," Acta Biomater. **60**, 64–80 (2017).
[4]M. Mullender, A. E. Haj, Y. Yang, M. Van Duin, E. Burger, and J. Klein-Nulend, "Mechanotransduction of bone cells in vitro: Mechanobiology of bone tissue," Med. Biol. Eng. Comput. **42**, 14–21 (2004).
[5]A. Bakker, J. Klein-Nulend, and E. Burger, "Shear stress inhibits while disuse promotes osteocyte apoptosis," Biochem. Biophys. Res. Commun. **320**, 1163–1168 (2004).
[6]J. You, C. Yellowley, H. Donahue, Y. Zhang, Q. Chen, and C. Jacobs, "Substrate deformation levels associated with routine physical activity are less stimulatory to bone cells relative to loading-induced oscillatory fluid flow," J. Biomech. Eng. **122**, 387–393 (2000).
[7]E. Gamsjäger, C. M. Bidan, F. D. Fischer, P. Fratzl, and J. Dunlop, "Modelling the role of surface stress on the kinetics of tissue growth in confined geometries," Acta Biomater. **9**, 5531–5543 (2013).
[8]M. Rumpler, A. Woesz, J. W. Dunlop, J. T. Van Dongen, and P. Fratzl, "The effect of geometry on three-dimensional tissue growth," J. R. Soc. Interface **5**, 1173–1180 (2008).
[9]C. M. Nelson, R. P. Jean, J. L. Tan, W. F. Liu, N. J. Sniadecki, A. A. Spector, and C. S. Chen, "Emergent patterns of growth controlled by multicellular form and mechanics," Proc. Natl. Acad. Sci. **102**, 11594–11599 (2005).
[10]W. Jin, K.-Y. Lo, S.-E. Chou, S. W. McCue, and M. J. Simpson, "The role of initial geometry in experimental models of wound closing," Chem. Eng. Sci. **179**, 221–226 (2018).
[11]R. D. O'Dea, M. Nelson, A. E. Haj, S. L. Waters, and H. M. Byrne, "A multiscale analysis of nutrient transport and biological tissue growth in vitro," Math. Med. Biol. **32**, 345–366 (2015).
[12]R. O'Dea, H. Byrne, and S. Waters, "Continuum modelling of in vitro tissue engineering: A review," Comput. Model. Tissue Eng. **10**, 229–266 (2012).
[13]Y. Guyot, I. Papantoniou, Y. C. Chai, S. Van Bael, J. Schrooten, and L. Geris, "A computational model for cell/ECM growth on 3D surfaces using the level set method: A bone tissue engineering case study," Biomech. Model. Mechanobiol. **13**, 1361–1371 (2014).
[14]P. Sanaei, L. Cummings, S. Waters, and I. Griffiths, "Curvature-and fluid-stress-driven tissue growth in a tissue-engineering scaffold pore," Biomech. Model. Mechanobiol. **18**, 589–605 (2019).
[15]M. A. Alias and P. R. Buenzli, "Modeling the effect of curvature on the collective behavior of cells growing new tissue," Biophys. J. **112**, 193–204 (2017).
[16]P. Kumar, B. Dey, and G. R. Sekhar, "Nutrient transport through deformable cylindrical scaffold inside a bioreactor: An application to tissue engineering," Int. J. Eng. Sci. **127**, 201–216 (2018).
[17]P. Kumar and G. R. Sekhar, "Analysis of elastohydrodynamics and nutrient transport through deformable porous scaffold inside a hollow fiber membrane bioreactor," Phys. Fluids **32**, 031904 (2020).
[18]P. Kumar and G. R. Sekhar, "Elastohydrodynamics of a deformable porous packing in a channel competing under shear and pressure gradient," Phys. Fluids **32**, 061901 (2020).
[19]M. A. Alias and P. R. Buenzli, "A level-set method for the evolution of cells and tissue during curvature-controlled growth," Int. J. Numer. Methods Biomed. Eng. **36**, e3279 (2020).
[20]S. G. Hegarty-Cremer, M. J. Simpson, T. L. Andersen, and P. R. Buenzli, "Modelling cell guidance and curvature control in evolving biological tissues," J. Theor. Biol. **520**, 110658 (2021).
[21]F. Zhao, T. J. Vaughan, and L. M. McNamara, "Quantification of fluid shear stress in bone tissue engineering scaffolds with spherical and cubical pore architectures," Biomech. Model. Mechanobiol. **15**, 561–577 (2016).
[22]S. M. Giannitelli, D. Accoto, M. Trombetta, and A. Rainer, "Current trends in the design of scaffolds for computer-aided tissue engineering," Acta Biomater. **10**, 580–594 (2014).
[23]A. Cheng, Z. Schwartz, A. Kahn, X. Li, Z. Shao, M. Sun, Y. Ao, B. D. Boyan, and H. Chen, "Advances in porous scaffold design for bone and cartilage tissue engineering and regeneration," Tissue Eng. Part B: Rev. **25**, 14–29 (2019).
[24]A. Rouhollahi, O. Ilegbusi, S. Florczyk, K. Xu, and H. Foroosh, "Effect of mold geometry on pore size in freeze-cast chitosan-alginate scaffolds for tissue engineering," Ann. Biomed. Eng. **48**, 1090–1102 (2020).
[25]J. L. Drury and D. J. Mooney, "Hydrogels for tissue engineering: Scaffold design variables and applications," Biomaterials **24**, 4337–4351 (2003).
[26]N. C. Pearson, R. J. Shipley, S. L. Waters, and J. M. Oliver, "Multiphase modelling of the influence of fluid flow and chemical concentration on tissue growth in a hollow fibre membrane bioreactor," Math. Med. Biol. **31**, 393–430 (2014).
[27]M. Shakeel, P. C. Matthews, R. S. Graham, and S. L. Waters, "A continuum model of cell proliferation and nutrient transport in a perfusion bioreactor," Math. Med. Biol. **30**, 21–44 (2013).
[28]C. Chung, C. Chen, C. Chen, and C. Tseng, "Enhancement of cell growth in tissue-engineering constructs under direct perfusion: Modeling and simulation," Biotechnol. Bioeng. **97**, 1603–1616 (2007).
[29]G. Lemon, J. R. King, H. M. Byrne, O. E. Jensen, and K. M. Shakesheff, "Mathematical modelling of engineered tissue growth using a multiphase porous flow mixture theory," J. Math. Biol. **52**, 571–594 (2006).
[30]G. I. Taylor, "Dispersion of soluble matter in solvent flowing slowly through a tube," Proc. R. Soc. London Ser. A. Math. Phys. Sci. **219**, 186–203 (1953).
[31]P. Sanaei and L. J. Cummings, "Flow and fouling in membrane filters: Effects of membrane morphology," J. Fluid Mech. **818**, 744 (2017).
[32]S. Y. Liu, Z. Chen, and P. Sanaei, "Effects of particles diffusion on membrane filters performance," Fluids **5**, 121 (2020).
[33]K. P. Kommareddy, C. Lange, M. Rumpler, J. W. Dunlop, I. Manjubala, J. Cui, K. Kratz, A. Lendlein, and P. Fratzl, "Two stages in three-dimensional in vitro growth of tissue generated by osteoblastlike cells," Biointerphases **5**, 45–52 (2010).
[34]R. D. O'Dea, S. L. Waters, and H. M. Byrne, "A multiphase model for tissue construct growth in a perfusion bioreactor," Math. Med. Biol. **27**, 95–127 (2010).
[35]R. J. Shipley and S. L. Waters, "Fluid and mass transport modelling to drive the design of cell-packed hollow fibre bioreactors for tissue engineering applications," Math. Med. Biol. **29**, 329–359 (2012).
[36]H. Suhaimi and D. B. Das, "Glucose diffusivity in cell-seeded tissue engineering scaffolds," Biotechnol. Lett. **38**, 183–190 (2016).
[37]R. J. McMurtrey, "Analytic models of oxygen and nutrient diffusion, metabolism dynamics, and architecture optimization in three-dimensional tissue constructs with applications and insights in cerebral organoids," Tissue Eng. Part C: Methods **22**, 221–249 (2016).
[38]M. P. Dalwadi, M. Bruna, and I. M. Griffiths, "A multiscale method to calculate filter blockage," J. Fluid Mech. **809**, 264–289 (2016).

[39]M. P. Dalwadi, I. M. Griffiths, and M. Bruna, "Understanding how porosity gradients can make a better filter using homogenization theory," Proc. R. Soc. A: Math. Phys. Eng. Sci. **471**, 20150464 (2015).
[40]Z. Chen, S. Y. Liu, I. C. Christov, and P. Sanaei, "Flow and fouling in elastic membrane filters with hierarchical branching pore morphology," Phys. Fluids **33**, 062009 (2021).
[41]A. Dana, Z. Zheng, G. G. Peng, H. A. Stone, H. E. Huppert, and G. Z. Ramon, "Dynamics of viscous backflow from a model fracture network," J. Fluid Mech. **836**, 828–849 (2018).
[42]V. Anand and I. C. Christov, "Transient compressible flow in a compliant viscoelastic tube," Phys. Fluids **32**, 112014 (2020).
[43]K. Raj M, J. Chakraborty, S. DasGupta, and S. Chakraborty, "Flow-induced deformation in a microchannel with a non-Newtonian fluid," Biomicrofluidics **12**, 034116 (2018).
[44]C. M. Bidan, K. P. Kommareddy, M. Rumpler, P. Kollmannsberger, P. Fratzl, and J. W. Dunlop, "Geometry as a factor for tissue growth: Towards shape optimization of tissue engineering scaffolds," Adv. Healthcare Mater. **2**, 186–194 (2013).